

Automatic Segmentation of Optic Disc in Eye Fundus Images: A Survey

Ali Mohamed Nabil Allam^{*}, Aliaa Abdel-Halim Youssif[†], Atef Zaki Ghalwash[‡]

^{*} *College of Management & Technology, Arab Academy for Science & Technology, Cairo, Egypt*

^{†,‡} *Faculty of Computers and Information, Helwan University, Cairo, Egypt*

Received 20th Sep 2014; accepted 7th Apr 2015

Abstract

Optic disc detection and segmentation is one of the key elements for automatic retinal disease screening systems. The aim of this survey paper is to review, categorize and compare the optic disc detection algorithms and methodologies, giving a description of each of them, highlighting their key points and performance measures. Accordingly, this survey firstly overviews the anatomy of the eye fundus showing its main structural components along with their properties and functions. Consequently, the survey reviews the image enhancement techniques and also categorizes the image segmentation methodologies for the optic disc which include property-based methods, methods based on convergence of blood vessels, and model-based methods. The performance of segmentation algorithms is evaluated using a number of publicly available databases of retinal images via evaluation metrics which include accuracy and true positive rate (i.e. sensitivity). The survey, at the end, describes the different abnormalities occurring within the optic disc region.

Keywords: optic disc, image enhancement, image segmentation, medical image processing, optic disc abnormalities

1. Introduction

It is known that ophthalmologists all over the world rely on eye fundus images in order to diagnose and treat various diseases that affect the eye. Therefore, experts have been applying digital image processing techniques to retinal images with the main aim of identifying, locating, and analyzing the retinal landmarks which are the optic disc, the macula, and the blood vessels. This computer-aided image analysis, in turn, facilitates the detection of retinal lesions and abnormalities which significantly affect the general appearance and semblance of the retinal landmarks. Hence, the early detection of abnormalities which affect the fundus such as exudates, aneurysms, hemorrhages, and the change in shape and size of the blood vessels and/or the optic disc, leads to diagnosing and predicting other serious pathological conditions that the eye may suffer from such as diabetic retinopathy, macular edema, glaucoma (ocular hypertension), and blindness.

Fundus, Latin for the word "bottom", is an anatomical term referring to the portion of an organ opposite from its opening. Hence, the fundus of the eye is the interior surface of the eye, opposite the lens, and includes the retina, optic disc, macula and fovea, and posterior pole [1]. The eye's fundus is the only organ of the central nervous system of the human body that can be imaged directly since it can be seen through the pupil [1] and [2]. Therefore, numerous numbers of fundus images of the retina are analyzed by ophthalmologists all over the world, and over the past two decades experts have been applying digital image processing techniques to ophthalmology with the main aim of improving diagnosis of various diseases that affect the eye such as diabetic retinopathy, aneurysms, arteriosclerosis, glaucoma, hemorrhages, neovascularization, etc. [1] and [2]. Some of the functions performed by the interior surface of the human eye, along with their semblance and characteristics, are described below:

Correspondence to: ali.allam@staff.aast.edu

<http://dx.doi.org/10.5565/rev/elcvia.680>

Recommended for acceptance by Jorge Bernal

ELCVIA ISSN: 1577-5097

Published by Computer Vision Center / Universitat Autònoma de Barcelona, Barcelona, Spain

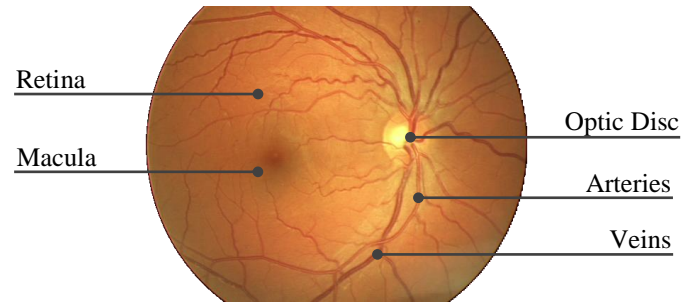


Figure 1. Eye fundus image

- **Retina:** contains light sensitive cells called cones and rods, which are responsible for daytime and night vision, respectively; the retina is the tissue where the image is projected since it receives images formed by the lens and converts them onto signals that reach the brain by the means of the optic nerve. The color of the retina varies naturally according to the color of the light employed; however, the color of the normal fundus may be described as ranging from orange to vermillion [2].
- **Optic Disc:** also called the optic nerve head or papilla. This is a circular area where the optic nerve enters the retina; it does not contain receptors itself, and thus it is the blind spot of the eye. The optic disc is round or vertically oval in shape, measuring about 2mm in diameter, and typically appears as a bright yellowish or white area. Also, large blood vessels are found in the vicinity of the optic disc [2], [3].
- **Macula & Fovea:** the macula is a part of the eye close to the center of the retina which allows us to see objects with great detail. The fovea is a depression in the retina that contains only cones (not rods), and which provides accurate focused eyesight. The fovea, which falls at the center of the area known as the macula, is an oval-shaped, blood vessel-free reddish spot. It is approximately 5mm from the center of the optic disc (equal to about 2.5 times the diameter of the optic disc) [2].
- **Blood Vessels:** like the rest of the human body, arteries and veins are the two main types of blood vessels responsible for the blood supply. Arteries carry fresh blood from the heart and lungs to the eye while veins take away the blood that has been used by the eye and return it to the lungs and heart to be refreshed with oxygen and other nutrients [4]. The major branches of the retinal vasculature originate from the center of the optic disc to the four quadrants of the retina. In the macular region, all the vessels arch around, sending only small branches towards the vascular fovea area. The arteries appear with a brighter red color and are slightly narrower than the veins [2].

2. Image Processing for Ophthalmology

The majority of works dealing with ophthalmology image processing can be divided into two broad categories [2] [5]:

2.1. Automated Detection of Abnormalities

This group aims at identifying the abnormalities in the retina in order to assist ophthalmologists to diagnose, predict and monitor the progress of, the disease that a patient suffers from.

- **Disease diagnosis:** refers to detecting the abnormal symptoms in the retina such as exudates, aneurysms and hemorrhages in order to diagnose diseases that affect the eye like diabetic retinopathy, glaucoma, macular edema, etc.
- **Disease prediction:** refers to observing the retinal disorders that may lead to other pathological conditions or vision loss (blindness).
- **Disease progress monitoring:** concerned with comparing the changes of the states in the eye fundus at particular intervals of time in order to observe either the improvement or deterioration of some disease.

2.2. Automated Segmentation of Landmarks

The eye fundus is being segmented in order to locate and isolate the retinal landmarks, namely the optic disc, macula, fovea, veins and arteries.

- **Optic disc segmentation:** the optic disc is a key landmark in retinal images, and shows changes related to diseases including glaucoma and diabetic retinopathies. The optic disc also serves as a landmark in order to locate other fundus features such as the macula and blood vessels [3] as mentioned before in section 1.
- **Macula and fovea segmentation:** locating the macula is important in detecting related diseases such as macular degeneration and macular edema [5].
- **Vascular segmentation (veins & arteries):** analyzing the blood vessels in the retina is important for detection of diseases of blood circulation such as diabetic retinopathy.

3. System Architecture of Retinal Image Processing

Figure 2 proposes the high-level system architecture of retinal image processing showing the data which is employed, the steps which are followed and the procedures which are applied in processing the eye fundus images.

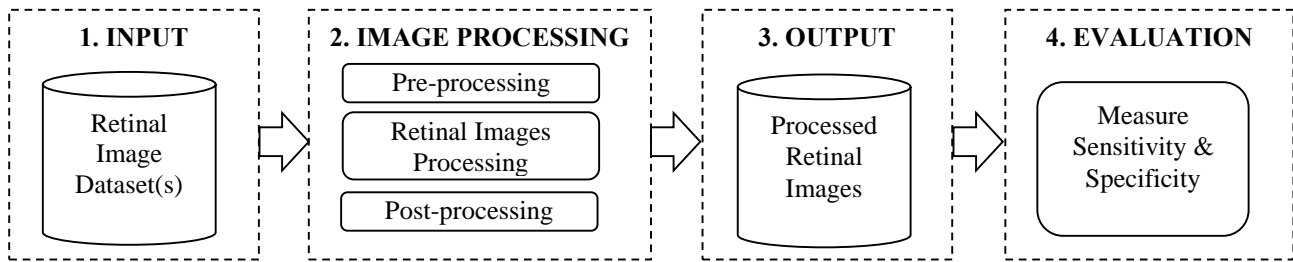


Figure 2. Architecture of retinal image processing

Each of the four components of the system architecture is briefly described below, and then discussed in detail in the subsequent sections:

- Input – retinal image datasets (section 4): refers to one set or more of retinal images that form the input data to be processed.
- Image processing (section 6): this is the backbone of the system architecture which is composed usually of three sub-processes in order to manipulate the dataset of the raw retinal images and convert it to a set of meaningful images (e.g. diagnosing a retinal image that suffers from a particular disease):
 - i. Preprocessing (section 6): a preliminary step that normally aims to enhancing the input image (e.g. contrast, sharpness and illumination of the image).
 - ii. Retinal images processing (section 7): the main objective of processing the retinal image normally aims to the segmentation of the image which is the process of isolating particular regions of interest within the image [6]. Regions of interest (ROI) may include retinal abnormalities (e.g. exudates, hemorrhages, aneurysms, etc.), and may also include the retinal landmarks (e.g. optic disc, macula, and vascular tree) as discussed earlier at section 2.
 - iii. Post-processing: refers to the last processing step that aims to describing and marking (i.e. annotating) either the external boundary or the internal skeleton of the objects/regions that were segmented in the fundus image.
- Output – processed retinal images: the output dataset which refers to the retinal images after being enhanced, processed and then annotated. These processed retina images are compared to the ground truth in order to evaluate the accuracy of experimental work.
- Evaluation (section 5): the accuracy of experimental results is measured by estimating indices for the true positive, true negative, false positive, and false negative.

4. Retinal Image Datasets

The retinal images are considered as the raw material to be enhanced, segmented and evaluated. Image datasets are normally accompanied with a ground truth which acts as a benchmark for comparing and evaluating the achieved experimental results using the true results provided usually by medical experts (i.e. ophthalmologists) on an image dataset. Table 1 shows a chronological list of the most widely used datasets of retinal images employed for optic disc image processing, in particular.

Table 1. Retinal images datasets

Dataset Name	Dataset Size	FOV	Image Size (pixels)	Images Format	Ground Truth
STARE (2000)	397 images	35°	700 × 605	PPM	Blood Vessels and Optic Disc
DRIVE (2004)	40 images (two sets)	45°	565 × 584 (both sets)	TIFF	Blood Vessels
MESSIDOR (2004)	1200 images (three sets)	45°	Set(1): 1440 × 960 Set(2): 2240 × 1488 Set(3): 2304 × 1536	TIFF	Retinopathy Grading and Macular Edema (Hard Exudates)
ONHSD (2004)	99 images	45°	760 × 570	BMP	Optic Disc
ARIA (2006)	143 images (three sets)	50°	768 × 576	TIFF	Vessels, Optic Disc and Fovea
ImageRet (2008)	Diaretdb0: 130 images Diaretdb1: 89 images	50°	1500 × 1152	PNG	Microaneurysms, Hemorrhages, and Hard & Soft Exudates

There are other more publicly available databases, such as REVIEW, HRF and ROC, which are not described here as they are not commonly used by researchers in optic disc segmentation, as noticed in section 7. A more detailed description of the most widely used publicly available datasets described in the table above, along with an explanation of their ground truth, is overviewed below:

4.1. STARE

Dataset description: STARE dataset (**S**tructured **A**nalysis of the **R**etina) [7] contains 397 raw images captured using a fundus camera with a field of view (FOV) of 35 degrees. Each image is of size of 700×605 pixels, with 24 bits per pixel; the images have been clipped at the top and the bottom of the FOV.

Ground truth: each image within the dataset is diagnosed as pertaining to one or more of thirteen different abnormalities, in which blood vessel segmentation experimental work is provided including 40 hand-labeled images, along with the experimental results, and a demo. Also optic disc detection work including 81 images is also provided along with ground truth, and the experimental results.

4.2. DRIVE

Dataset description: DRIVE database (**D**igital **R**etinal **I**mages for **V**essel **E**xtraction) [8] has been developed for comparative studies on segmentation of blood vessels in retinal images. The dataset contains 40 images in which 33 do not show any sign of diabetic retinopathy and 7 show signs of mild early diabetic retinopathy. Each image was captured using 8 bits per color plane at 565×584 pixels with a FOV of 45 degrees. For this database, the images have been cropped around the FOV, and for each image, a mask image is provided that delineates the FOV.

Ground truth: the set of 40 images has been divided into a training set and a test set, both containing 20 images. For the training images, a single manual segmentation of the vasculature is available. For the test cases, two manual segmentations are available; one is used as gold standard, the other one can be used to compare computer generated segmentations with those of an independent human observer. The DRIVE's website provides a results page that lists results from some algorithms in a tabular format. The result browser is a useful way to explore the database by viewing images and segmentations for a small set of methods that had been implemented.

4.3. MESSIDOR

Dataset description: MESSIDOR database (**M**éthodes d'**E**valuation de **S**ystèmes de **S**egmentation et d'**I**ndexation **D**édiées à l'**O**phthalmologie **R**étinienne) [9] has been established to facilitate studies on computer-assisted diagnoses of diabetic retinopathy. The dataset contains 1200 images packaged in three sets. Each set is divided into four subsets, each of which containing 100 images in TIFF format. The images were captured acquired using a camera with a 45 degree field of view using 8 bits per color plane at 1440×960, 2240×1488 and 2304×1536 pixels. 800 images were acquired with pupil dilation (one drop of Tropicamide at 0.5%) and 400 without dilation.

Ground truth: each set is associated with a spreadsheet that includes two diagnoses which are the retinopathy grade and the risk grade of macular edema provided by medical experts for each image. The retinopathy grade is classified into four grades (grade 0, 1, 2 and 3) according to three main factors which are the number of microaneurysms, number of hemorrhages, and the neovascularization. On the other hand, hard exudates have been used to classify the risk of macular edema into three grades (grade 0, 1 and 2).

4.4. ONHSD

Dataset description: ONHSD dataset (**O**ptic **N**erve **H**ead **S**egmentation **D**ataset) [10] contains 99 fundus images taken from 50 patients randomly sampled from a diabetic retinopathy screening program; 96 images have discernible Optic Nerve Head (ONH). The images were acquired using a fundus camera with a field angle lens of 45 degrees and size of 760×570 pixels. Images were converted to gray-scale by extracting the intensity component from the HSI representation. There is considerable quality variation in the images, with many characteristics that can affect segmentation algorithms.

Ground truth: the ONH center has been marked up by a clinician. Then, four clinicians marked the ONH edge where it intersects with radial spokes (at 15 degree angles) radiating from the nominated center. These multiple nominations of the edge are used to characterize the degree of subjective uncertainty in the edge position.

4.5. ARIA

Dataset description: ARIA (**A**utomated **R**etinal **I**mage **A**nalysis) [11], [12] aims to provide an automated image capture and image analysis platform capable of predicting individuals at risk of eye disease. The dataset contains a total of 143 images collected by staff members of St. Paul's Eye Unit and the University of Liverpool as part of the ARIA project. The images are captured with a camera of FOV of 50 degrees at resolution of 768×576 and stored as uncompressed TIFF files. The dataset is organized into three groups, including 23 images of age-related macular degeneration, 61 images healthy control-group, and 59 diabetic images.

Ground truth: Two image analysis experts have traced out the blood vessels in the images of all three groups. Also, the locations of the optic disk and fovea have also been outlined in the diabetic and healthy control groups.

4.6. ImageRet

Dataset Description: ImageRet database [13] is divided into two subsets, DIARETDB0 and DIARETDB1, which are used for benchmarking diabetic retinopathy detection. The ImageRet dataset was made publicly available in 2008 using a digital fundus camera of 50 degrees field of view in which each image is of size of 1500×1152 pixels in PNG format. The DIARETDB0 subset contains 130 retinal images of which 20 are normal and the other 110 images contain various symptoms of diabetic retinopathy, whereas DIARETDB1 contains 89 color fundus images of which 84 contain at least mild non-proliferative signs (i.e. microaneurysms) of the diabetic retinopathy, and 5 are considered as normal which do not contain any signs of the diabetic retinopathy.

Ground truth: For every fundus image there is a corresponding ground truth file. A ground truth file contains all finding types found in the specific image, namely, red small dots (i.e. microaneurysms), hemorrhages, hard exudates, soft exudates, and neovascularization.

5. Evaluation Metrics

Although the evaluation of an algorithm normally comes at the final stage of a detection and segmentation method, yet the metrics used for evaluation are reviewed here in advance, in order to provide a concrete understanding of the results achieved by the segmentation algorithms in the literature which will be reviewed consequently in section 7.

In medical diagnosis, the region of interest ROI (i.e. landmark or lesion) is usually classified into two classes: present or absent; in which the response given by a human observer (expert) or a computer process is: positive or negative. Therefore, the detection of the ROI is normally depicted using the terms presented in Table 2 [14]. The evaluation of the medical imaging test is usually determined by estimating indexes for the true positive (T_P), true negative (T_N), false positive (F_P), false negative (F_N).

Table 2. Signal detection indices and derived evaluation metrics

	Present ROI	Absent ROI
Positive Response	Hit (T_P)	False alarm (F_P)
Negative Response	Miss (F_N)	Correct rejection (T_N)
	$SENS = \frac{T_P}{T_P + F_N}$	$SPEC = \frac{T_N}{T_N + F_P}$

The T_P and T_N indices refer to the successful response in detecting and rejecting region of interests, respectively. The true positive index (T_P) indicates the positive response of a human observer or computer for the ROI that is present within the retina, while the true negative index (T_N) indicates the negative response for a landmark or abnormality that is not present. On the other hand, the F_P and F_N indices refer to an unsuccessful rejection and detection, respectively. The false positive index (F_P) indicates the positive response for the ROI that is not present, whereas the false negative index (F_N) indicates the negative response for the ROI that is present.

Derived from the four aforementioned indices as shown in Table 2, four statistical metrics are computed in order to evaluate the detection of landmarks or abnormalities, which are: sensitivity, specificity, positive predictive value, and negative predictive value.

5.1. Sensitivity and Specificity

Sensitivity is a measure that reflects the probability of a positive response for the cases in which the landmark or abnormality is present, whereas specificity is the probability of negative response for the cases in which the landmark or abnormality is absent. Both, sensitivity and specificity are expressed either as a proportion or a percentage given by the equation shown in Table 2, in which sensitivity and specificity are sometimes referred to as true positive rate and true negative rate, respectively. Moreover, the term false positive rate (FPR) is also used for the complement of specificity, computed as $(1 - \text{specificity})$ [15].

5.2. Segmentation Accuracy

Normally, the spatial features of an object of interest such as its size, shape and area are the parameters that are commonly used in order to evaluate the segmentation accuracy of an object of interest. Moreover, these parameters also have clinical significance because they help in diagnosing and treating diseases, as well as assessing the effect of treatment. Therefore, the main requirement needed to evaluate the segmentation results is the presence of the ground truth which is manually-defined by human observers indicating the true features of the segmented object (i.e. its true size, shape or area). Thus, once the ground truth data is available, a variety of metrics can be used to evaluate the segmentation process. These evaluation metrics include the Hausdorff distance and the degree of overlap, which are relatively easy to compute and at the same time are not limited to certain geometrical patterns [16]. Other pixel-wise metrics such as the

Euclidean distance is sometimes used to measure similarity, but the main drawback of such metric is that the similarity is estimated according to the distance between only two pixels such as the distance between the centroid of two optic discs.

Hausdorff Distance

The intuition behind Hausdorff distance is to measure the similarity between two sets. So, if these sets have close Hausdorff distance, they are considered to look almost the same. Therefore, the Hausdorff distance $h(A, B)$ is used to measure the similarity between two contours of the same object (e.g. optic disc), in which one contour A is defined by a human expert while the other contour B is generated by a computer process. The Hausdorff distance is computed as follows [16], [17]:

Let $A = \{a_1, a_2, \dots, a_m\}$ and $B = \{b_1, b_2, \dots, b_m\}$ be the set of points on the two contours in which each point represents a pair of x and y coordinates. Then, the distance of a point a_i to the closest point on curve B is defined as

$$d(a_i, B) = \min_j \|b_j - a_i\| \quad (1)$$

Similarly, the distance of a point b_j to the closest point on curve A is given by

$$d(b_j, A) = \min_i \|a_i - b_j\| \quad (2)$$

Finally, the Hausdorff distance is defined as the maximum of the above distances between the two contours.

$$h(A, B) = \max \left[\max_i \{d(a_i, B)\}, \max_j \{d(b_j, A)\} \right] \quad (3)$$

Overlap Score

The degree of overlap between two areas G and E encompassed by contours A and B , respectively, is defined as the ratio of the intersection and the union of these two areas, where G is the ground truth human-defined area and E is the experimental computer-generated area. The degree of overlap is computed as follows [16], [18], [19]:

$$OL = \frac{G \cap E}{G \cup E} \quad (4)$$

If there is an exact overlap between both contours, the ratio will be 1, whereas the ratio is given by 0 if there is no overlap between the two contours.

6. Preprocessing Functions: Image Enhancement

As mentioned before, image processing is the main component of the system architecture which includes three sub-processes in order to manipulate the dataset of the captured retinal images and convert it to a set of meaningful images. The input image is first enhanced, then segmented, and finally annotated. Software packages such as MATLAB[®] and ImageJ[®] provide a powerful means for implementing these image processing functions.

Unfortunately, the raw digital fundus images are not always ready for immediate processing because of their poor quality due to factors such as the patient's movement and iris color, as well as imaging conditions such as non-uniform illumination. Therefore, an image should be first preprocessed in order to make it more suitable for further processing. The following subsections present the main preprocessing functions.

6.1. Mask Generation

A fundus image consists of a semi-oval region of interest (ROI) on a dark background which is never really pure black (i.e. non-zero intensity). Therefore, masks are created and used in order to exclude the dark background of the image from further calculations and processing; in other words, only the pixels belonging to the semi-oval retinal fundus are included for processing. The mask image is a binary image in which the background pixels are assigned the value of "zero" and pixels within the ROI are assigned the value of "one", where the original color image is multiplied by the created mask image to produce a color image without noisy pixels in the background, while the ROI is left unchanged [20], as shown in Figure 3.

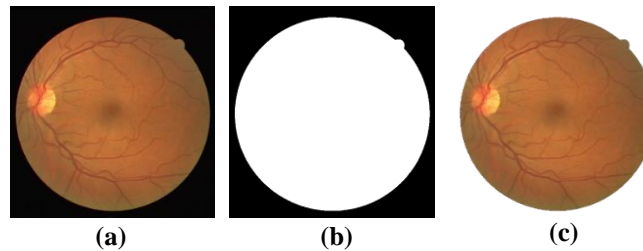


Figure 3. Mask generation

(a) A color image, (b) its corresponding mask, and (c) its excluded background

However, some of the publicly available retinal datasets, such as DRIVE, HRF, DIARETDB0 and DIARETDB1, are accompanied with the corresponding mask images, but most of the other datasets do not include such mask images, and therefore the retinal images must be manipulated in some way in order to generate their corresponding masks.

For instance, in their procedure of detecting the anatomical structures in fundus images, Gagnon *et al.* [21] generated the mask image using pixel value statistics outside the ROI of the fundus image which were calculated for each of the three color bands. Consequently, a 4-sigma thresholding was applied such that pixels with intensity value above that threshold were considered to belong to the ROI. Finally, results for all bands were combined through logical operations and region connectivity test in order to identify the largest common connected mask, since ROI size was not always the same for each band due to different color response of the camera.

Also, Goatman *et al.* [22] automatically generated the masks by the simple thresholding of the green channel of the retinal image followed by a 5×5 median filtering in order to exclude the dark surrounding region.

Ter Haar [20] created the mask by thresholding the red channel of the retinal image using a threshold value that was determined empirically, and then the thresholded image was morphologically processed via the opening, closing and erosion operators through a 3×3 square kernel.

In the same direction, Hashim *et al.* [23] generated the binary mask by convolving the red channel with a Gaussian low-pass filter, in which the resultant image was thresholded using Otsu's global threshold.

6.2. Color Channels Processing

The retinal fundus color image consists of three channels, in which the green channel has the highest contrast, whereas the red channel tends to be saturated and it is the brightest channel, while the blue channel tends to be empty [24], as shown in Figure 4.

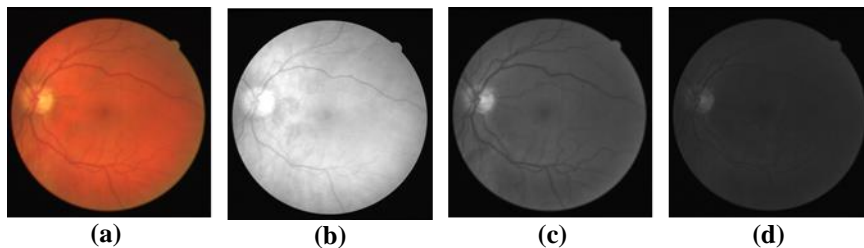


Figure 4. (a) Full-color image split into its (b) RED, (c) GREEN and (d) BLUE channels

Because it provides the highest contrast, the green channel has been extensively exploited by most algorithms, discarding the red component in some cases “so-called red-free images” and ignoring the blue component in most, or even all, algorithms. Therefore, the green channel was utilized for miscellaneous purposes such as detecting different retinal landmarks and several abnormalities due to its high contrast within retinal images. For instance, Hoover and Goldbaum [24] located the optic disc using only the green band of the retinal image, whereas Staal *et al.* [8] used the green channel for the extraction of image ridges in color fundus images, while Niemeijer *et al.* [25] localized both the optic disc and fovea simultaneously using only the green plane of the color fundus image.

However, even though the green channel was utilized solely in most approaches and for different purposes as mentioned in the previous paragraph, yet the red channel was also exploited sometimes in combination with the green band. For instance, Aquino *et al.* [19] observed that the optic disc appeared in the red field as a well-defined white shape, brighter than the surrounding area, and therefore, the optic disc segmentation was performed in parallel on the red and green bands and the better of the two segmentations was ultimately selected. Also, Lu [18] and Hashim *et al.* [23] combined intensity information from the red and green channels together by calculating a modified intensity channel component using a weighted average, in which a higher weight was given to the red channel in order to keep the image variation across the optic disc boundary but suppress that across the retinal vessels.

6.3. Color Normalization

Another major preprocessing task in retinal images is color normalization which does not aim to find the true color of an image, but in fact color normalization algorithms transform the color of an image so as to be invariant with respect to the color of illumination, without losing the ability to differentiate between the objects or regions of interest [22]. The most frequently-used algorithms for color normalization are the gray-world normalization, comprehensive normalization, histogram equalization and histogram specification.

Gray-world normalization, also referred to as gray-world assumption algorithm, assumes that the changes in the illuminating spectrum can be modeled by three multiplicative constants applied to the red, green and blue channels, respectively. The new color of any pixel is calculated by dividing each color channel by its respective mean value, removing the dependence on the multiplicative constant. Comprehensive normalization, a variation of the gray-world normalization proposed by Finlayson *et al.* [26], is a technique that iteratively applies chromaticity normalization followed by gray-world normalization for four or five iterations, until the change in values is less than a certain tolerance value.

On the other hand, histogram equalization is a non-linear transform applied individually to the red, green and blue bands of an image which affects the color perceived. It is considered to be a more powerful normalization transformation than the gray-world method. The results of histogram equalization tend to have an exaggerated blue channel and look unnatural due to the fact that in most images the distribution of the pixel values is usually more similar to a Gaussian distribution, rather than uniform [27].

Last but not least, histogram specification transforms the red, green and blue histograms to match the shapes of three specific histograms, rather than simply equalizing them, which results in more realistic images than those produced by equalization [22].

Both, Goatman *et al.* [22] and Youssif *et al.* [28] evaluated the effectiveness of the aforementioned methods of color normalization which aim to reduce color variations among different retinal images. According to the evaluation of Goatman *et al.* [22], histogram specification was found to be the most effective normalization method in clustering and discriminating four different types of lesions, namely the cotton wool spots, hard exudates, blot hemorrhages, and drusen. Moreover, histogram specification had the advantage that it produced more realistic looking images since it did not exaggerate the contribution of the blue channel like the other methods, as shown in Figure 5, whereas comprehensive normalization was not found to perform much better than gray-world normalization in discriminating the lesions.

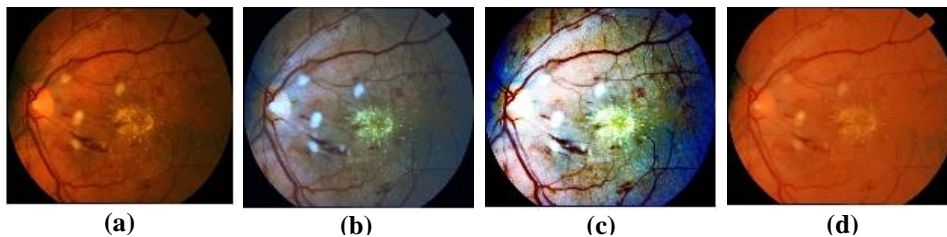


Figure 5. Effect of color normalization on abnormal retina

(a) Reference image (b) Gray-world normalization (c) Histogram equalization (d) Histogram specification

From a different perspective, Youssif *et al.* [28] evaluated normalization techniques by distinguishing vessels and non-vessels, as shown in Figure 6. Histogram specification recorded the worst result in discriminating the vessels from non-vessels, while histogram equalization was found to be the most effective method by showing a clear separation between clusters of vessels and non-vessels, whereas comprehensive normalization, compared to gray-world normalization, showed more intense clusters and a narrower overlap between objects scattered in both clusters.

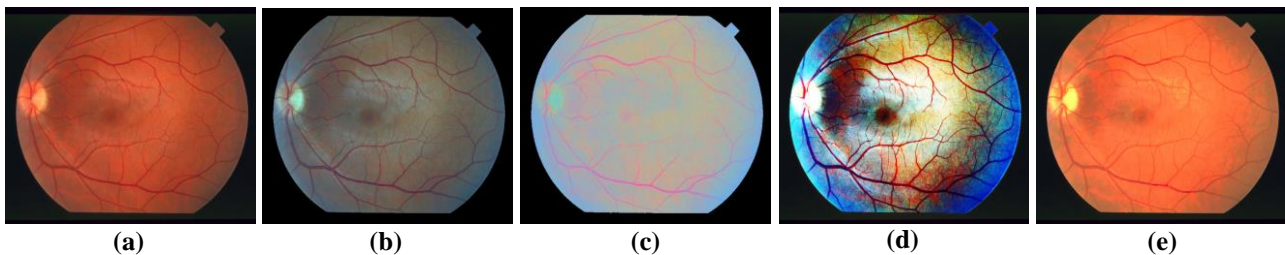


Figure 6. Effect of color normalization on vessels

(a) Reference image (b) Gray-world normalization (c) Comprehensive normalization
(d) Histogram equalization (e) Histogram specification

6.4. Contrast Enhancement

Contrast enhancement is the process of either darkening or brightening a low-contrast intensity image by spreading the range of intensities so that it spans the full range of intensity. Hence, some of the color normalization techniques, such as histogram equalization and histogram specification which were applied to the three color bands, may be also utilized to enhance the contrast of an image using one band only, typically the green channel, the one which provides the highest contrast between regions of interest and the retinal background as mentioned before. The main disadvantage of using histogram equalization (HE) in contrast enhancement is its dependence on the global statistics of an image, which may lead to noise amplification as well as the absence of some gray levels. This in turn results in a washed-out appearance in parts of the image due to over enhancement, while other parts around the periphery may not be enhanced enough [6], [29].

Adaptive histogram equalization (AHE), applied by Wu *et al.* [30] and also exploited by Youssif *et al.* [3] in enhancing the contrast, differs from the ordinary histogram equalization in the respect that the adaptive method computes several histograms, each of which corresponds to a distinct section of the image in order to redistribute the lightness values of the image. Therefore, it is suitable for improving the local contrast of an image and bringing out more detail, however noise may be still amplified as the ordinary histogram equalization. Fadzil *et al.* [31], Krishnan *et al.* [32] and Maruthusivarani *et al.* [33] enhanced the contrast of the retinal image using contrast-limited adaptive histogram equalization (CLAHE) which is an improved variation of the AHE that limits the amplification of noise produced by the standard AHE.

Figure 7 distinguishes the contrast of the green-band of an image using histogram equalization and CLAHE.

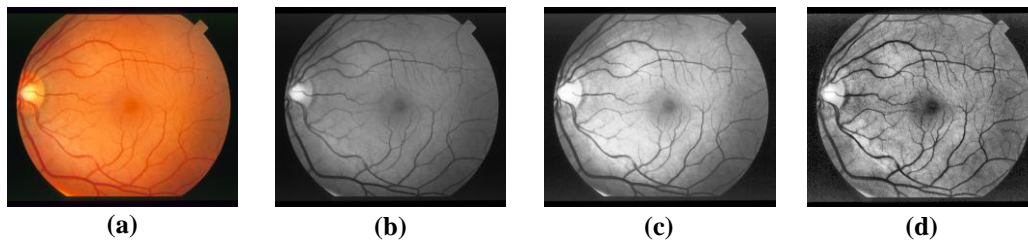


Figure 7. Contrast enhancement via HE and CLAHE

(a) Reference image (STARE: im0077.ppm)

(b) Green-band of (a) (c) Histogram Equalization of (b) (d) CLAHE of (b)

7. Optic Disc Segmentation

Detecting and locating the main anatomical structures of the retina, such as the optic disc, the macula, the fovea and the major blood vessels, is considered an essential step towards detecting abnormalities and analyzing lesions in the retinal images. Thus, these segmented retinal landmarks may be exploited to establish a coordinate system (retinal model) of the eye fundus which in turn may be used to determine the spatial relationship of lesions, edema and hemorrhages with reference to the optic disc and macula.

Properties of the optic disc

The optic disc is found towards the right-hand or left-hand side of a fundus image. It is round or vertically oval in shape, measuring about one-sixth the width of the image (i.e. approximately 2mm in diameter) which corresponds to about 80~100 pixels in a standard fundus image, and typically appears as a bright yellowish or white area. Also, the optic disc appears as the convergent area of the vascular tree of blood vessels [2], [3], [34], [35], [36].

Motivation of optic disc detection

Detecting the optic disc and analyzing its properties serves as an indicator of various ophthalmologic pathologies such as diabetic retinopathy and glaucoma. As because of the similarity and confusion between exudates and the optic disc (Figure 8-b), diabetic retinopathy can be diagnosed by isolating and omitting the optic disc which improves the identification of exudates, one of the main retinal abnormalities occurring in diabetic retinopathy [3], [37].

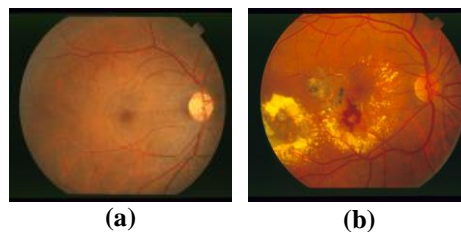


Figure 8. (a) Healthy retina (b) Diabetic retina (containing exudates)

The process of locating the optic cup aims only to identifying the centroid of the optic disc, whereas detecting the optic rim (neuroretinal rim) aims to identifying the boundary between the retina and the optic disc [3]. The ratio between the optic cup and neuroretinal rim surfaces (cup-to-disc ratio) is an important structural indicator for assessing the presence of glaucoma. Figure 9 distinguishes the optic cup and the optic rim within the optic disc.

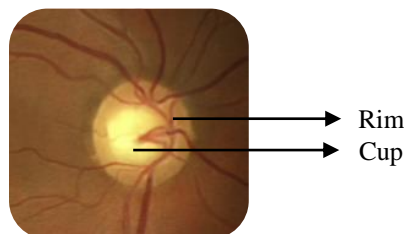


Figure 9. The cup and the rim of the optic disc

The pathology of glaucoma is characterized by the cupping of the optic disc which becomes ischemic due to the imbalance between the intraocular pressure and the perfusion pressure in the vessels of the retina [2], as shown in Figure 10.

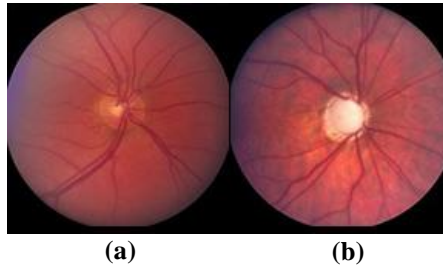


Figure 10. (a) Normal optic disc (b) Glaucomatous optic disc

Literature of optic disc detection

The main methods of optic disc detection reviewed in the literature are categorized and discussed in the following part:

7.1. Property-based methods

This category of methods is based directly on the above mentioned properties of the optic disc (e.g. location, size, color and shape). In the early work of the optic disc detection, Goldbaum *et al.* [38] utilized most of these properties in order to jointly locate the optic disc. They combined three properties of the optic disc: the convergence of blood vessels at the optic disc, the appearance of the optic disc as a bright region, and entrance of large vessels above and below the optic disc.

Also, Sinthanayothin *et al.* [34] located the optic disc by identifying the area with the highest variation in intensity of adjacent pixels using a window whose size equal to that of the optic disc. Their approach correctly detected the optic disc with sensitivity and specificity of 99.1% on a local dataset composed of 112 TIFF fundus images.

Similarly, based on the brightness and roundness of the optic disc, Park *et al.* [39] also presented a method with a successful detection percentage of 90.25% using an approach that included thresholding, detection of object roundness, and detection of circles.

Also, Chrástek *et al.* [40] applied an averaging filter to the green-band image, and roughly located the optic disc at the point with the highest average intensity with a success rate of 97.3% on a local dataset.

Walter and Klein [41] approximated the centroid of the optic disc as the center of the largest and brightest connected object in the fundus. Their method successfully detected optic disc in all images of a local dataset composed of 30 images, and achieved a success rate of 58% on the STARE dataset.

Carmona *et al.* [42] proposed a genetic algorithm in order to obtain an ellipse that approximated the optic disc. First, they obtained a set of hypothesis points that exhibited the geometric properties and intensity levels similar to the optic disc contour pixels. The genetic algorithm was used next to find an ellipse containing the maximum number of hypothesis points in an offset of its perimeter. The results of their algorithm showed that 96% of the 110 retinal images had less than five pixels of discrepancy.

Using the Circular Hough Transform, Abdel-Ghafar *et al.* [43] were able to detect the optic disc by finding the largest circular object. Similarly, Zhu *et al.* [44], [2] also used the Hough Transform to detect the circles in which the best-fitting circle for the optic disc was chosen by using a method of intensity-based selection. They achieved a successful detection rate of 90% on the DRIVE dataset and 44.4% on the STARE dataset.

A circular transformation was designed by Lu [18] to capture both the circular shape of the optic disc as well as the image variation across the optic disc boundary, simultaneously. The variation of each pixel within the retinal image was measured along multiple evenly-oriented radial line segments of specific length. The pixels with the maximum variation along all radial line segments were determined, which were then exploited to locate both the center and the boundary of the optic disc. Experimental results showed that the center of the optic disc was accurately detected in 99.75%, 97.5%, and 98.77% of the STARE, ARIA and MESSIDOR datasets, respectively. Also, the boundary of the optic disc was accurately segmented in 93.4% and 91.7% of the STARE dataset and the ARIA dataset, respectively.

Zubair *et al.* [45] detected the optic disc by increasing its contrast using preprocessing techniques such as CLAHE, contrast stretching transformation, and extended minima transformation. Using the contrasted image, the optic disc was localized by using morphological erosion and dilation in order to remove all non-optic disc regions that are not of the size of the optic disc. Finally, after taking negative of the image, the resultant image obtained was subtracted from the resized green-channel component to get an optic disc free image, with an accuracy of 98.65% on the MESSIDOR dataset.

Yu and Yu [46] localized the optic disc through a method based on extracting the brightest pixels, iteratively, in order to overcome the presence of any other bright artifacts such as large exudates. Initially, the image was smoothed via the Gaussian filter and then the blood vessels were removed from the image using the closing operator. Then, at each round in the iterative algorithm, the brightest pixels were extracted and a binary candidate map was constructed. Both, the thresholds for the area and the circular degree were employed in order to select and identify the optic disc region among other candidates. The proposed method successfully localized the optic disc in 95% of only 40 images from the STARE dataset.

7.2. Convergence of blood vessels

Instead of relying on the properties of the optic disc, an alternative approach to detect the optic disc is to exploit the information provided by the vascular tree of the retina, since the optic disc is considered as the convergence point of the few major blood vessels that split into many smaller vessels throughout the retina [3].

Taking advantage of this spatial relationship between the optic disc and blood vessels, Hoover and Goldbaum [24] developed a voting-type algorithm called fuzzy convergence in order to detect the origination of the blood-vessel network (i.e. convergence point) which was considered as the center of the optic disc in a fundus image. The input to their algorithm was a binary segmentation of the blood vessels, in which each vessel was modeled by a fuzzy segment that contributed to a cumulative voting image. The output of the algorithm was a convergence image which was thresholded to identify the strongest point(s) of convergence. This technique successfully detected 89% of the normal and abnormal images in the STARE dataset.

The Hough Transform was utilized by ter Haar [20] in two different ways. In the first method, the Hough Transform was applied only to the pixels on or close to the binary image of the retinal vasculature obtained by Staal *et al.* [8], in which the binary image was dilated in order to increase the number of optic disc candidates. This approach achieved a success rate of 96.3% on a local dataset and 71.6% on the STARE dataset. In the second alternative method, the Hough Transform was applied only to the brightest 0.35% of the fuzzy convergence image obtained by Hoover and Goldbaum [24], in which dilation was applied again to the convergence image to fill the gaps created by small vessels. This approach achieved a success rate of 97.4% on a local dataset and 65.4% on the STARE dataset.

Fleming *et al.* [47] detected the approximate region of the optic disc using an elliptical shape of the major retinal vessels which was formed using the Generalized Hough Transform. The approximate location of the optic disc was then refined via the Circular Hough Transform achieving a success rate of 98.4% of the 1056 retinal images, in which the positional accuracy was better than 50% of the diameter of the optic disc.

Ying *et al.* [48] proposed an algorithm that differentiates the optic disc from other bright regions such as hard exudates, in which the optic disc was detected based on its high fractal dimension of the converging pattern of blood vessels. With its location known, the optic disc was correctly segmented via local histogram analysis in 97.5% of the images of the DRIVE dataset.

Based on tensor voting for analyzing vessel structures, Park *et al.* [49] proposed a method to identify the location of the optic disc. The vessel patterns were first extracted by tensor voting in equalized images, and then the position of the optic disc was identified by mode detection which was based on mean-shift procedure. Their approach was tested with 90 images from the STARE dataset, which achieved 100% success rate on 40 normal images and 84% on pathological images.

In the work of Rangayyan *et al.* [50], [2], the blood vessels were first detected using Gabor filters, and then phase portrait modeling was applied to detect the convergence points of the vessels, in which the best-fitting circle for the optic disc was chosen by using an intensity-based condition. This approach achieved success rates of 100% and 69.1% for the DRIVE and STARE datasets, respectively.

7.3. Model-based methods (template-matching)

This type of methods is based on comparing a template image (model) with a set of candidates in order to determine the best-matching candidate. Lalonde *et al.* [17] implemented a Hausdorff-based template matching technique using edge maps, guided by pyramidal decomposition for large-scale object tracking where small bright lesions (e.g. exudates) disappear, creating fewer optic disc candidates. The edge map regions were matched to a circular template with different radii using the Hausdorff distance, and the region having the largest number of overlapped template pixels was considered the optic disc. This approach correctly detected the center of the optic disc in 93% of a dataset of 40 images.

Another model-based approach was proposed by Osareh *et al.* [51] who created a gray-level template image by averaging the optic disc region of 25 images whose colors were normalized using histogram specification. The center of the optic disc was located by using the generated template along with gray-scale morphological filtering and active-contour modeling in which the normalized correlation coefficient was used to find the most similar match between the template and all the candidate pixels, with an average accuracy of 90.32% in detecting the boundary of the optic disc of 75 images of the retina.

Also, Li and Chutatape [52] created an optic disc model (disc-space) by applying Principal Component Analysis (PCA) to a training set of 10 intensity normalized images that were manually cropped around the optic disc. The candidate regions with the highest 1% gray-level were selected and matched to the disc-space, in which the optic disc was successfully detected in 99% of the images as the region with the smallest Euclidean distance to its projection onto the disc-space.

Also, the method proposed by Foracchia *et al.* [53] for detecting the optic disc was based on a preliminary detection of the major retinal vessels. They proposed a geometrical model to describe the general direction of retinal vessels at any given position using the coordinates of the optic disc center which were two model parameters estimated by the means of a simulated annealing optimization technique. The position of the optic disc was correctly located in 97.53% of the STARE images using the common vertex of the two model parameters (i.e. the convergence point for the blood vessels).

Lowell *et al.* [10] designed a detection filter (i.e. template) for the optic disc which was composed of a Laplacian of Gaussian filter with a vertical channel carved out of the middle corresponding to the major blood vessels exiting the optic disc vertically. This template was then correlated to the intensity component of the fundus image using full Pearson-R correlation. The optic disc was successfully detected in 99% of the images in a local dataset.

A method presented by ter Haar [20] was based on fitting the vascular orientations on a directional model (DM), using a training set of 80 images of vessel segmentations. For all the pixels in each vessels image, the orientation was calculated to form a directional vessel map, in which the DM was created by averaging, at each pixel, all the corresponding orientation values in the directional maps. At the end, each pixel in an input vasculature was aligned to the center of the optic disc, and the pixel having the minimal distance to both DMs was selected as the optic disc location. This method detected the optic disc successfully in 99.5% of the images in a local dataset and 93.8% of the STARE dataset.

Closely related, Youssif *et al.* [3] proposed another model-based approach by matching the expected directional pattern of the retinal blood vessels found in the vicinity of the optic disc. They obtained a vessels direction map of the retinal vessels that were segmented using 2D Gaussian matched filter. The minimum difference between the matched filter and the vessels directions at the surrounding area of each of the optic disc candidates achieved a successful detection rate of 100% on the DRIVE dataset and 98.77% on the STARE dataset.

Niemeijer *et al.* [25] formulated the problem of finding a certain position in a retinal image as a regression problem. A k-nearest neighbor classifier (k-NN) was trained to predict the distance to the optic disc given a set of measurements of the retinal vasculature obtained around a circular template placed at a certain location in the image. The method was trained with 500 images for which the location of the optic disc was known, where the point with the lowest predicted distance to the optic disc was selected as the optic disc center. This supervised method was tested using 600 images of which 100 images contained gross abnormalities, and successfully located the optic disc in 99.4% of the normal images and 93% of the pathological images.

Aquino *et al.* [19] presented a template-based methodology that used morphological and edge detection techniques followed by the Circular Hough Transform to obtain an approximate circular optic disc boundary. Their methodology required an initial pixel located within the optic disc, and for this purpose, a location procedure based on a voting-type algorithm was utilized and succeeded in 99% of the cases. The algorithms were evaluated on the 1200 images of the MESSIDOR dataset, achieving a success rate of 86%.

Lu [54] used another technique for the detection of the optic disc in a way different than the one he used in [18] (previously reviewed in the section 7.1). In the proposed technique, the retinal background surface was first estimated through an iterative Savitzky-Golay smoothing procedure. Afterwards, multiple optic disc candidates were detected through the difference between the retinal image and the estimated retinal background surface. Finally, the real optic disc was selected through the combination of the difference image and the directional retinal blood vessel which was based on the observation that the retinal blood vessels were mostly oriented vertically as they exit the optic disc. The proposed technique was evaluated over four datasets DIARETDB0, DIARETDB1, DRIVE and STARE giving an accuracy of 98.88%, 99.23%, 97.50% and 95.06%, respectively.

Instead of creating an image and using it as a template, Deghani *et al.* [35] constructed three histograms as a template for localizing the center of the optic disc using four retinal images from the DRIVE dataset, in which each histogram represented one color channel. Then, an 80×80 window was moved through the retinal image to obtain the histogram of each channel. Finally, they calculated the correlation between the histogram of each channel in the moving window and the histograms of its corresponding channel in the template. The DRIVE, STARE, and a local dataset composed of 273 images were used to evaluate their proposed algorithm, in which the success rate was 100%, 91.36% and 98.9%, respectively.

Lately, [55] proposed a method for detecting the optic disc accurately in an efficient way. First, the algorithm identified a number of possible vertical windows (x-coordinates) for the optic disc according to three characteristics of retinal vessels, which are: (1) the high density of vessels at optic disc vicinity, (2) compactness of the vertical vascular segments around the optic disc center, and (3) the uniform distribution of vessels. Consequently, the y-coordinate of the optic disc is identified according to the vessels direction via parabola curve fitting using the General Hough Transform. The proposed method was tested on four datasets: DIARETDB0, DIARETDB1, DRIVE and STARE, in which the optic disc was correctly detected in all images of each dataset, except only one image in the STARE dataset.

Table 3 compares all the aforementioned methods for optic disc segmentation in a chronological order, along with datasets employed in each and their corresponding sensitivity and accuracy results.

Table 3. List of optic disc detection methods

#	Approach	Dataset	SENS	ACC
1	Goldbaum <i>et al.</i> , (1996) [38]: Vessels convergence, optic disc brightness, and entrance of large vessels	None	-	-
2	Sinthanayothin <i>et al.</i> , (1999) [34]: High intensity variation	Local dataset (112 images) STARE (81 images) ¹	0.9911 0.4200	- -
3	Lalonde <i>et al.</i> , (2001) [17]: Hausdorff template matching & pyramidal decomposition	Local dataset (40 images) STARE (81 images) ¹	1.0000 0.7160	0.9300 -
4	Walter & Klein, (2001) [41]: Largest brightest connected object	Local dataset (30 images) STARE (81 images) ¹	0.9000 0.5800	- -
5	Chrastek <i>et al.</i> , (2002) [40]: Highest average intensity	Local dataset (261 images)	0.9732	0.8171
6	Osareh <i>et al.</i> , (2002) [51]: Averaged OD-images template matching	Local dataset (75 images) STARE (81 images) ¹	0.9032 0.5800	- -
7	Hoover & Goldbaum, (2003) [24]: Fuzzy convergence of vessels	STARE (81 images)	0.8900	-
8	Foracchia <i>et al.</i> , (2004) [53]: Geometrical model of vessel structure	STARE (81 images)	0.9753	-
9	Li & Chutatape, (2004) [52]: Template matching via PCA	Local dataset (89 images)	0.9900	0.9400
10	Lowell <i>et al.</i> , (2004) [10]: OD Laplacian of Gaussian template & full Pearson-R correlation	Local dataset (90 images)	0.9900	-
11	ter Haar, (2005) [20]: Hough Transform applied to the pixels on or close to the retinal vasculature	STARE (81 images) Local dataset (191 images)	0.7160 0.9634	- -
12	ter Haar, (2005) [20]: Hough Transform applied to the fuzzy convergence image	STARE (81 images) Local dataset (191 images)	0.6543 0.9738	- -
13	ter Haar, (2005) [20]: Fitting the vasculature orientations on a directional model	STARE (81 images) Local dataset (191 images)	0.9948 0.9383	- -
14	Park <i>et al.</i> , (2006) [39]: Brightness and roundness detection	DRIVE (40 images)	0.9025	-
15	Abdel-Ghafar <i>et al.</i> , (2007) [43]: Circular Hough Transform	None	-	-
16	Fleming <i>et al.</i> , (2007) [47]: Elliptical form of blood vessels	Local dataset (1056 images)	0.9840	-
17	Park <i>et al.</i> , (2007) [49]: Tensor voting and adaptive mean-shift	STARE (90 images)	0.8400	-
18	Ying <i>et al.</i> , (2007) [48]: Fractal dimension of blood vessels and local histogram analysis	DRIVE (40 images)	0.9750	-
19	Carmona, (2008) [42]: Approximating elliptical form of optic disc via genetic algorithm	Local dataset (110 images)	0.9600	-
20	Youssif <i>et al.</i> , (2008) [3]: Vessels' direction matched filter	DRIVE (40 images) STARE (81 images)	1.0000 0.9877	- -
21	Niemeijer <i>et al.</i> , (2009) [25]: Vasculature measurements and the k-NN regression	Local dataset (600 images)	0.9300	-
22	Aquino <i>et al.</i> , (2010) [19]: Morphology, edge detection and circular Hough transform	MESSIDOR (1200 images)	0.9900	0.8600
23	Lu, (2010) [54]: Estimation of retinal background surface and directional blood vessel information	DIARETDB0 (130 images) DIARETDB1 (89 images) DRIVE (40 images) STARE (81 images)	0.9888 0.9923 0.9750 0.9506	- - - -
24	Rangayyan <i>et al.</i> , (2010) [50]: Vessels convergence by Gabor filters and phase portrait modelling	DRIVE (40 images) STARE (81 images)	1.000 0.6910	- -
25	Zhu <i>et al.</i> , (2010) [44]: Circle detection via Hough transform	DRIVE (40 images) STARE (81 images)	0.9000 0.4440	- -
26	Lu, (2011) [18]: Circular transformation and image variation along multiple radial line segments	ARIA (120 images) MESSIDOR (1200 images) STARE (81 images)	0.9750 0.9975 0.9877	0.9170 - 0.9340

¹ Additional results for the STARE dataset were obtained from the comparative study done by ter Haar, 2005.

#	Approach	Dataset	SENS	ACC
27	Dehghani <i>et al.</i> , (2012) [35]: Histogram-based template matching	DRIVE (40 images)	1.0000	-
		Local dataset (273 images)	0.9890	-
		STARE (81 images)	0.9136	-
28	Zubair <i>et al.</i> , (2013) [45]: Contrast enhancement and morphological transformation	MESSIDOR (1200 images)	1.0000	0.9865
29	Yu & Yu, (2014) [46]: Iterative brightest pixels extraction	STARE subset (40 images)	0.9500	-
30	Zhang & Zhao, (2014) [55]: Vessels distribution and directional characteristics	DIARETDB0 (130 images)	1.0000	-
		DIARETDB1 (89 images)	1.0000	-
		DRIVE (40 images)	1.0000	-
		STARE (81 images)	0.9877	-

8. Abnormalities within the Optic Disc

The detection of abnormalities, such as microaneurysms, exudates, and hemorrhages can assist in the diagnosis of retinopathy [2]. Diabetic retinopathy and diabetic maculopathy affect the retinal periphery and the retinal center (macula), respectively. Besides, glaucoma is another retinal disease that affects the optic disc (i.e. intra-papillary region) and the area surrounding it (i.e. peripapillary region). There are five main different types of glaucoma, namely, open-angle, normal-tension, closed-angle, congenital, and secondary glaucoma [56]. Typically, glaucoma can be detected through the following clinical indicators within the intra-papillary and peripapillary regions: (1) Large Cup-to-disc ratio, (2) Thickness of neuroretinal rim violates the ISNT rule, (3) Defect of the retinal nerve fiber layer, (4) Appearance of optic disc hemorrhages, (5) Existence of peripapillary atrophy. [57], [58], [59], [60], [61], [62], [63], [64].

8.1. Cup-to-Disc Ratio (CDR)

The CDR is defined as the ratio of the vertical diameter of the optic cup to the vertical diameter of the neuroretinal rim (NRR) which is an important structural indicator for assessing the presence of glaucoma characterized by the cupping of the optic disc, as shown earlier in Figure 10. Clinically, glaucoma is suspicious with a CDR more than 0.6. However, the CDR in one eye is not always a reliable indicator due to the varying cup size among patients. Therefore, a glaucomatous optic cup can be identified more precisely via the relative cupping asymmetry between the left eye and right eye, where the asymmetry between the sizes of the two cups is typically more than 0.2 [57], [65].

8.2. ISNT Rule

In addition to the CDR ratio, glaucoma is also diagnosed via the incompliance of the NRR's thickness with the ISNT rule (Inferior / Superior / Nasal / Temporal), in which the normal optic disc typically demonstrates a configuration where the inferior neuroretinal rim is the widest portion of the rim, followed by the superior rim, and then the nasal rim, and finally the temporal rim which is the narrowest [59], [60], [61], as shown in Figure 11 [66].

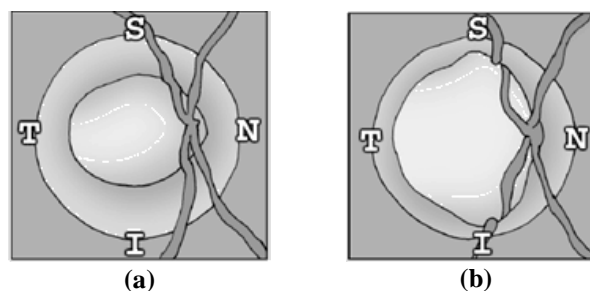


Figure 11. Sketch of the ISNT rule for the thickness of the neuroretinal rim

(a) Healthy neuroretinal rim – follows the ISNT rule

(b) Glaucomatous neuroretinal rim – violates the ISNT rule

8.3. Nerve Fiber Layer Defect (NFLD)

The retinal nerve fiber layer (NFL) is formed by the ganglion cell axons; and it represents the innermost layer of the eye fundus. Due to the loss of ganglion cells, it is well known that the NFLD precedes and subsequently leads to the enlargement of the optic cup; and hence the NFLD is considered one of the earliest signs of glaucoma [67]. The NFL is best observed using red-free or green light images where the normal healthy eye has a thick layer of retinal nerve fibers which can be seen as fine bright striations (strips). The NFL demonstrates a “bright-dark-bright” pattern when viewed up from the superior-temporal region down to the inferior-temporal region. In other words, the retina shines in the regions in which the NFL is thickest (i.e. superior-temporal and inferior-temporal regions), whereas the area between the disc and

the macula (i.e. temporal region) appears darker [57], [58], [68]. Figure 12-a shows an example of the bright striations around the superior and inferior parts in a healthy retina creating the bright-dark-bright pattern [68].

On the other hand, the region around the optic disc with NFLD gets darker and changes from stripy-texture to wedge-shaped form. Also, blood vessels appear darker with sharp reflexes in the region of NFLD, as shown in Figure 12-b [68].

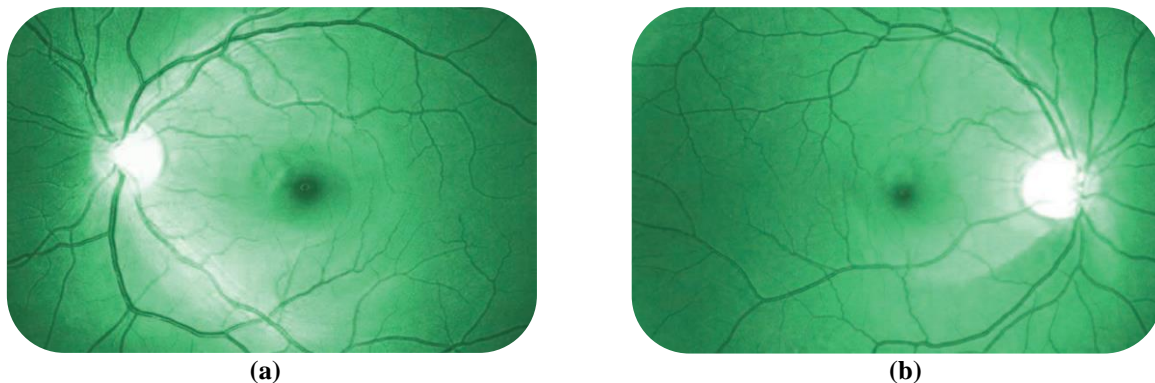


Figure 12. Red-free optic disc image showing nerve fiber layer

(a) Normal NFL: bright-dark-bright strip pattern (b) NFLD below the optic disc

There are two kinds of NFLD, namely, localized and diffuse. The localized NFLD appears as a wedge-shaped dark area that follows the pattern of the NFL originating from the optic disc [57], [58]. In such defects, the specificity is very high but the sensitivity is low since these defects are a definite sign of pathology, but can occur in diseases other than glaucoma [57]. On the other hand, diffuse NFLD can be seen in advanced glaucoma. It is usually more difficult to be detected in one eye, but it is easily recognized when both eyes are compared together. In diffuse NFLD, there is a general reduction of the NFL brightness causing the normal “bright-dark-bright” pattern to be lost and look like a “dark-dark-dark” pattern (i.e. appears completely dark) [57], [58], [68].

8.4. Disc Hemorrhages

Another important clinical indicator of glaucoma is the presence of splinter-like hemorrhages within the optic disc whose existence is more common in normal-tension glaucoma, compared to all other types of glaucoma. Moreover, disc hemorrhaging most often occurs in the same areas of, and also associated with, rim notching and NFLD (i.e. within the inferior-temporal and superior-temporal regions). Besides, the color of disc hemorrhages depends upon how long they have been present, since they are transient, lasting from two to six months, but may repeatedly occur [58], [62]. Figure 13 shows different examples of optic disc hemorrhages which have many appearances, depending on how long they have been present.

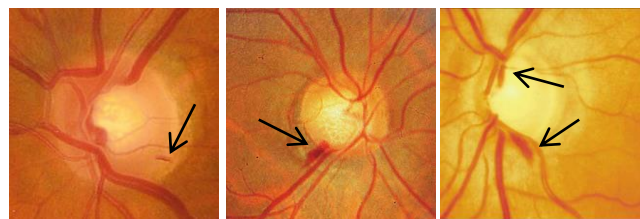


Figure 13. Optic disc splinter hemorrhages

8.5. Peripapillary Atrophy (PPA)

The peripapillary region, as its name implies, is the area located around the periphery of the papilla (i.e. just outside the optic disc). Thus, the peripapillary atrophy (PPA) refers to the thinning and degeneration of the chorioretinal tissue around the optic disc. Two distinct zones of atrophy, zone alpha (α) and zone beta (β) can surround the optic disc, in which zone alpha is located on the outer surface of zone beta, if present. The outer zone alpha is present in most normal eyes as well as the glaucomatous ones, characterized by a region of irregular hypo- and hyperpigmentation of the retinal pigment epithelium (RPE); whereas the inner zone beta is more often observed in glaucomatous eyes than in healthy eyes, which is caused by the atrophy of the RPE and choriocapillaris leaving intact choroid vasculature. The area of PPA is located and correlated within the region of NRR loss, with the atrophy being largest in the corresponding area of thinner NRR [58].

9. Discussion & Conclusion

The performance of the segmentation methods were normally compared via evaluation metrics such as sensitivity and accuracy. The following bar charts illustrate and distinguish the segmentation algorithms in terms of sensitivity with respect to the employed datasets. The algorithms are also classified and grouped into three categories: vessels-convergence methods (blue bars), property-based methods (orange bars), and template-based methods (red bars):

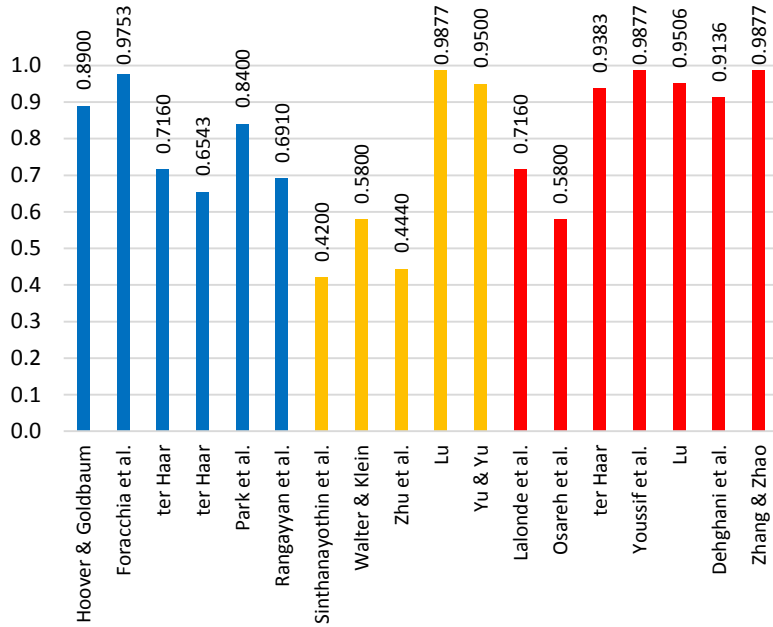


Figure 14. Sensitivity of algorithms over STARE

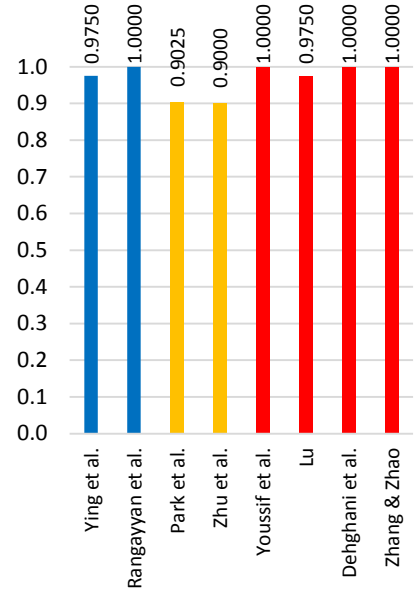


Figure 15. Sensitivity of algorithms over DRIVE

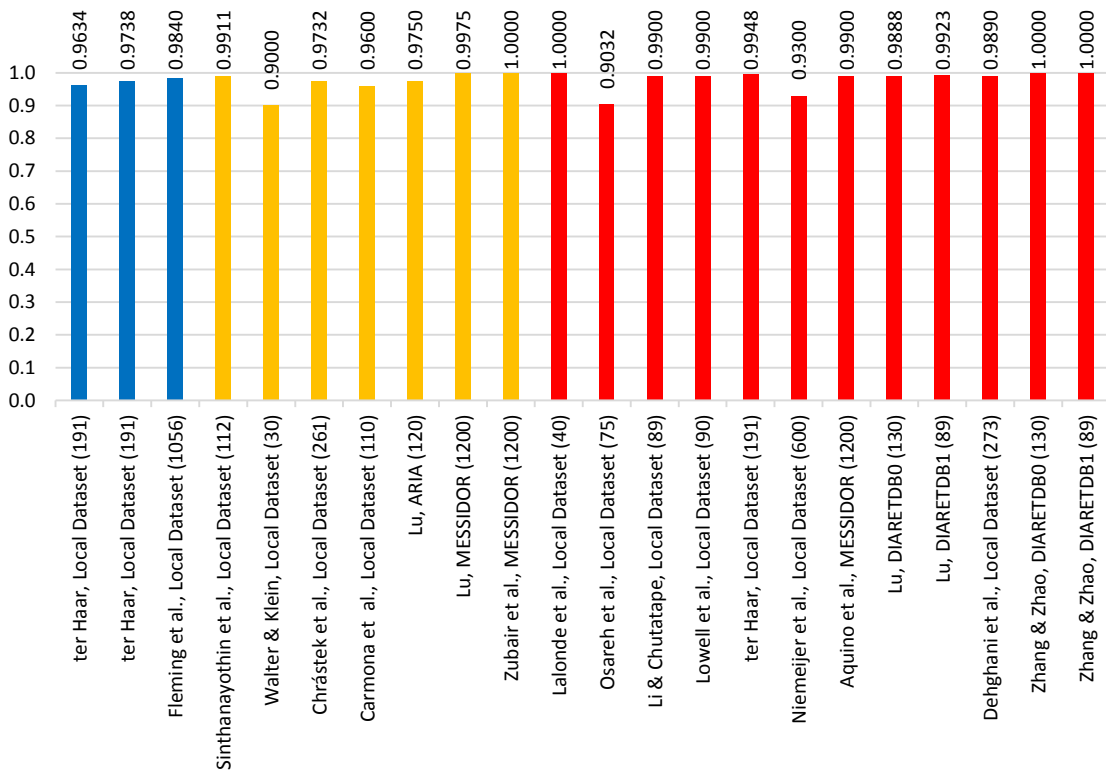


Figure 16. Sensitivity of algorithms over miscellaneous datasets

Moreover, the following conclusions are observed from the perspective of each stage of the optic disc image processing:

- **Image Datasets**

From the perspective of the datasets employed to segment the optic disc and evaluate their results, the STARE and DRIVE datasets were considered as the gold standard for most of the proposed segmentation algorithms. However, other more datasets such as MESSIODOR and DIARETDB0, and DIARETDB1 were also used infrequently by some of the algorithms. It was observed that segmentation algorithms achieve better results using the DRIVE dataset compared to that achieved with the STARE dataset. This is because of the good-quality images in the DRIVE dataset compared to the scanned images in the STARE dataset, as well as the presence of bright lesions within many of the STARE images.

- **Image Preprocessing**

Obviously, the preprocessing techniques potentially lead to “faster” and “more accurate” results at the further segmentation stage. For instance, the fundus images in most of the presented algorithms were initially masked out via a binary image in order to discard the dark background from further unnecessary processing. Also, in order to provide the highest contrast for an image, most algorithms extensively exploited the green channel of the image while other fewer ones used the red channel, whereas the blue channel was almost never used. Also, some algorithms exploited the intensity channel in the HSI color model. Moreover, this contrasted-image was re-enhanced using techniques such as histogram equalization and its variations (e.g. AHE and CLAHE), as well as other techniques that increase the sharpness of the ridges, such as unsharp masking, wavelet, contourlet, and curvelet transforms. These latter sharpening techniques proved to be more useful in enhancing the contrast of retinal vessels but they were comparative in enhancing the contrast of the optic disc.

- **Image Segmentation**

The optic disc segmentation approaches, in this survey, were categorized into: property-based methods, blood vessels-convergence methods, and template-matching methods. As a concluding observation, it was obvious that the methods based on the properties of the optic disc (e.g. its circular shape, brightness, size, etc.) achieved good results in normal fundus images that contained no abnormalities, but such approaches usually failed to detect the optic disc in pathological images where abnormalities, such as large exudates, were confused with the optic disc due to their similar appearance.

As a result, alternative approaches were followed by researchers in order to detect the optic disc without solely relying on the properties of the optic disc. These approaches exploited the information provided by the vascular tree of the retina, since the optic disc is considered as the convergence point of the major blood vessels. Moreover, other approaches relied on creating a template image (model) based on the optic disc properties along with the blood vessels properties (e.g. orientations, convergence, width, etc.), in order to determine the best-matching optic disc candidate. These approaches based on vessels-convergence and template matching proved to achieve better sensitivity rates than that achieved by the property-based methods, since the number of false responses were greatly reduced in the presence of other similar abnormal artifacts. But, on the other hand, such approaches obviously take more processing time than property-based methods.

- **Evaluation Metrics**

From the perspective of evaluating the segmentation techniques, all the proposed segmentation algorithms were evaluated in terms of the sensitivity rates (i.e. the true positive rates of detecting the optic disc). A few of these algorithms also provided the accuracy percentage of the segmented optic disc, while the specificity rates were rarely provided due to its insignificance because it is the probability of a negative response for the cases where the optic disc was absent, or more precisely, not apparent.

- **Diagnosis of Glaucomatous Optic Disc**

Last but not least, glaucoma can be detected through some abnormal indicators within the intra-papillary region (i.e. inside the optic disc itself), such as the large cup-to-disc ratio and the neuroretinal rim that violates the ISNT rule. Also, glaucoma can be detected through abnormalities occurring within the peripapillary region (i.e. the area surrounding the optic disc), such as the defect of the retinal nerve fiber layer, the appearance of optic disc hemorrhages, and the existence of peripapillary atrophy.

10. Summary

This survey reviewed the process of detecting and segmenting the optic disc, showing and comparing the techniques and methodologies that were followed for that purpose. It started by showing the publicly available databases for retinal images. The paper then compared the techniques used to enhance the raw fundus images, such as the contrast enhancement, illumination correction, mask generation, etc. At the end, the survey categorized the methods used for segmenting the optic disc, which were classified into property-based, vessels-convergence, and template-matching methods. Finally, the survey described the abnormalities that occur within the glaucomatous optic disc.

References

- [1] K. Mahesh K. and K. Nilesh S., "Review on Fundus Image Acquisition Techniques with Database Reference to Retinal Abnormalities in Diabetic Retinopathy," *Int. J. Comput. Applicat.*, vol. 68, no. 8, pp. 17-27, 2013.
- [2] X. Zhu, R. M. Rangayyan and A. L. Ells, "Digital Image Processing for Ophthalmology: Detection of the Optic Nerve Head," in *Synthesis Lectures on Biomedical Engineering*, Morgan & Claypool Publishers, 2011.
- [3] A. A. A. Youssif, A. Z. Ghalwash and A. A. S. A. Ghoneim, "Optic Disc Detection From Normalized Digital Fundus Images by Means of a Vessels' Direction Matched Filter," *IEEE Trans. Med. Imag.*, vol. 27, no. 1, pp. 11-18, 2008. DOI: 10.1109/TMI.2007.900326
- [4] Royal National Institute of Blind People (RNIB), "Retinal vessel occlusion," 7 August 2013. [Online]. Available: http://www.rnib.org.uk/eyehealth/eyeconditions/eyeconditionsoz/Pages/retinal_vessel_occlusion.aspx. [Accessed 19 August 2013].
- [5] N. Patton, T. M. Aslam, T. MacGillivray, I. J. Deary, B. Dhillon, R. H. Eikelboom, K. Yogesan and I. J. Constable, "Retinal image analysis: Concepts, applications and potential," *Progress in Retinal and Eye Research*, vol. 25, pp. 99-127, 2006. DOI: 10.1016/j.preteyeres.2005.07.001
- [6] R. C. Gonzalez and R. E. Woods, *Digital Image Processing*, Pearson Prentice Hall, 2008.
- [7] M. Goldbaum, "The STARE Project," 2000. [Online]. Available: <http://www.parl.clemson.edu/~ahoover/stare/index.html>. [Accessed 28 July 2013].
- [8] J. J. Staal, M. D. Abramoff, M. Niemeijer, M. A. Viergever and B. van Ginneken, "Ridge Based Vessel Segmentation in Color Images of the Retina," *IEEE Trans. Med. Imag.*, vol. 23, pp. 501-509, 2004. DOI: 10.1109/TMI.2004.825627
- [9] MESSIDOR - TECHNO-VISION Project, "MESSIDOR," 28 March 2008. [Online]. Available: <http://messidor.crihan.fr>. [Accessed 31 July 2013].
- [10] J. Lowell, A. Hunter, D. Steel, B. Ryder and E. Fletcher, "Optic Nerve Head Segmentation," *IEEE Trans. Med. Imag.*, vol. II, no. 23, 2004. DOI: 10.1109/TMI.2003.823261
- [11] Y. Zheng, M. H. A. Hijazi and F. Coenen, "Automated 'Disease/No Disease' Grading of Age-Related Macular Degeneration by an Image Mining Approach," *Investigative Ophthalmology & Visual Science*, vol. 53, no. 13, pp. 8310-8318, November 2008. DOI: 10.1167/iovs.12-9576
- [12] D. J. J. Farnell, F. N. Hatfield, P. Knox, M. Reakes, S. Spencer, D. Parry and S. P. Harding, "Enhancement of blood vessels in digital fundus photographs via the application of multiscale line operators," *J. Franklin Institute*, vol. 345, no. 7, pp. 748-765, October 2008. DOI: 10.1016/j.patrec.2006.09.007
- [13] ImageRet Project, Janaury 2008. [Online]. Available: <http://www.it.lut.fi/project/imageret/>.
- [14] E. M. Beytas, J. F. Debatin and R. A. Blinder, "Accuracy and predictive value as measures of imaging test performance," *Invest. Radiol.*, vol. 27, no. 5, pp. 374-378, May 1992.
- [15] P. Macaskill, C. Gatsonis, J. Deeks, R. Harbord and Y. Takwoingi, "Analysing and Presenting Results," in *Cochrane Handbook for Systematic Reviews*, J. Deeks, P. Bossuyt and C. Gatsonis, Eds., The Cochrane Collaboration, 2010.
- [16] M. Kallergi, "Evaluation Strategies for Medical-Image Analysis and Processing Methodologies," in *The Electrical Engineering and Applied Signal Processing Series: Medical Image Analysis Methods*, L. Costaridou, Ed., Taylor & Francis Group, 2005.
- [17] M. Lalonde, M. Beaulieu and L. Gagnon, "Fast and Robust Optic Disc Detection Using Pyramidal Decomposition and Hausdorff-Based Template Matching," *IEEE Trans. Med. Imag.*, vol. 20, no. 11, pp. 1193-1200, November 2001. DOI: 10.1109/42.963823
- [18] S. Lu, "Accurate and Efficient Optic Disc Detection and Segmentation by a Circular Transformation," *IEEE Trans. Med. Imag.*, vol. 30, no. 12, pp. 2126-2133, December 2011. DOI: 10.1109/TMI.2011.2164261
- [19] A. Aquino, M. E. Gegúndez-Arias and D. Marín, "Detecting the Optic Disc Boundary in Digital Fundus Images Using Morphological, Edge Detection, and Feature Extraction Techniques," *IEEE Trans. Med. Imag.*, vol. 29, no. 11, pp. 1860-1869, November 2010. DOI: 10.1109/TMI.2010.2053042
- [20] F. ter Haar, "Automatic localization of the optic disc in digital colour images of the human retina," 2005.
- [21] L. Gagnon, M. Lalonde, M. Beaulieu and M.-C. Boucher, "Procedure to detect anatomical structures in optical fundus images," in *Proc. SPIE Vol. 4322, Medical Imaging 2001: Image Processing*, 2001.
- [22] K. A. Goatman, A. D. Whitwam, A. Manivannan, J. A. Olson and P. F. Sharp, "Colour Normalisation of Retinal Images," *Proc. Medical Image Understanding Analysis*, 2003.
- [23] F. A. Hashim, N. M. Salem and A. F. Seddik, "Preprocessing of Color Retinal Fundus Images," in *IEEE 2013 2nd Int. Japan-Egypt Conf. Electron. Commun. Comput.*, 2013. DOI: 10.1109/JEC-ECC.2013.6766410

- [24] A. Hoover and M. Goldbaum, "Locating the Optic Nerve in a Retinal Image Using the Fuzzy Convergence of the Blood Vessels," *IEEE Trans. Med. Imag.*, vol. 22, no. 8, pp. 951-958, 2003. DOI: 10.1109/TMI.2003.815900
- [25] M. Niemeijer, M. D. Abramoff and B. van Ginneken, "Fast detection of the optic disc and fovea in color fundus photographs," *Med Image Anal.*, vol. 13, no. 6, pp. 859-870, December 2009. DOI: 10.1016/j.media.2009.08.003
- [26] G. D. Finlayson, B. Schiele and J. L. Crowley, "Comprehensive Color Image Normalization," in *Proc. 5th European Conf. Comput. Vision*, Freiburg, 1998.
- [27] W. Burger and M. J. Burge, *Digital Image Processing - An Algorithmic Introduction Using Java*, Springer London, 2008.
- [28] A. A. A. Youssif, A. Z. Ghalwash and A. S. Ghoneim, "A Comparative Evaluation of Preprocessing Methods for Automatic Detection of Retinal Anatomy," in *Proc. 5th Int. Conf. Informatics & Systems*, Cairo, 2007.
- [29] A. A. S. A. Ghoneim, "Artificial Intelligence Techniques for Ocular Pattern Classification," Cairo, 2007.
- [30] D. Wu, M. Zhang, J. Liu and W. Bauman, "On the Adaptive Detection of Blood Vessels in Retinal Images," *IEEE Trans. Biomed. Eng.*, vol. 53, no. 2, pp. 341-343, February 2006. DOI: 10.1109/TBME.2005.862571
- [31] M. H. A. Fadzil, L. I. Izhar, H. Nugroho and H. A. Nugroho, "Analysis of retinal fundus images for grading of diabetic retinopathy severity," *Med Biol Eng Comput*, January 2011. DOI: 10.1007/s11517-011-0734-2
- [32] M. R. Krishnan, U. R. Acharya, C. K. Chua, L. C. Min, E. Y. K. Ng, M. M. Mushrif and A. Laude, "Application of Intuitionistic Fuzzy Histon Segmentation for the Automated Detection of Optic Disc in Digital Fundus Images," in *Proc. IEEE-EMBS Int. Conf. Biomedical Health Informatics*, Hong Kong and Shenzhen, 2012. . DOI: 10.1109/BHI.2012.6211611
- [33] M. Maruthusivarani, T. Ramakrishnan, D. Santhi and K. Muthukkutti, "Comparison of Automatic Blood Vessel Segmentation Methods in Retinal Images," in *2013 Int. Conf. Emerging Trends VLSI Embedded Sys. Nano Electron. Telecommun. Syst.*, Tiruvannamalai, 2013. DOI: 10.1109/ICEVENT.2013.6496569
- [34] C. Sinthanayothin, J. F. Boyce, H. L. Cook and T. H. Williamson, "Automated localisation of the optic disc, fovea, and retinal blood vessels from digital colour fundus images," *British J. Ophthalmology*, vol. 4, no. 83, pp. 902-910, 1999. DOI: 10.1136/bjo.83.8.902
- [35] A. Dehghani, H. A. Moghaddam and M. Moin, "Optic disc localization in retinal images using histogram matching," *EURASIP J. Image Video Process.*, pp. 1-11, October 2012.
- [36] P. C. Siddalingaswamy, "Automatic Detection of Retinal Features for Screening of Diabetic Retinopathy using Image Processing Techniques," 2011.
- [37] G. Schaefer and A. Clos, "Image Analysis for Exudate Detection in Retinal Images," in *Biocomputation and Biomedical Informatics: Case Studies and Applications*, Medical Information Science Reference, 2010, pp. 198-203.
- [38] M. Goldbaum, S. Moezzi, A. Taylor, S. Chatterjee, J. Boyd, E. Hunter and R. Jain, "Automated diagnosis and image understanding with object extraction, object classification, and inferencing in retinal images," in *Proc. IEEE Int. Congr. Image Process.*, 1996.
- [39] M. Park, J. S. Jin and S. Luo, "Locating the Optic Disc in Retinal Images," in *Proc. 3rd Int. Conf. Computer Graphics, Imaging Visualization*, Sydney, Australia, 2006. DOI: 10.1109/CGIV.2006.63
- [40] R. Chrástek, M. Wolf, K. Donath, G. Michelson and Niemann, "Optic Disc Segmentation in Retinal Images," in *Bildverarbeitung für die Medizin 2002*, Springer Berlin Heidelberg, 2002, pp. 263-266. DOI: 10.1007/978-3-642-55983-9_60
- [41] T. Walter and J. Klein, "Segmentation of Color Fundus Images of the Human Retina: Detection of the Optic Disc and the Vascular Tree Using Morphological Techniques," in *Proc. 2nd Int. Symp. Medical Data Analysis (ISMDA '01)*, 2001. DOI: 10.1007/3-540-45497-7_43
- [42] E. J. Carmona, M. Rincon, J. Garcia-Feijoo and J. M. Martinez-de-la-Casa, "Identification of the optic nerve head with genetic algorithms," *Artificial Intell. Medicine*, vol. 43, no. 3, pp. 243-259, April 2008. DOI: 10.1016/j.artmed.2008.04.005
- [43] A. D. Abdel-Ghafar and T. Morris, "Progress towards automated detection and characterization of the optic disc in glaucoma and diabetic retinopathy," *Med. Inform. Internet Med.*, vol. 32, no. 1, pp. 19-25, March 2007. . DOI: 10.1080/14639230601095865
- [44] X. Zhu, R. M. Rangayyan and A. L. Ells, "Detection of the Optic Nerve Head in Fundus Images of the Retina Using the Hough Transform for Circles," *J. Digital Imaging*, vol. 23, no. 3, pp. 332-341, June 2010. DOI: 10.1007/s10278-009-9189-5
- [45] M. Zubair, A. Yamin and S. A. Khan, "Automated Detection of Optic Disc for the Analysis of Retina Using Color Fundus Image," in *IEEE Int. Conf. Imaging Syst. Techniques*, Beijing, 2013. DOI: 10.1109/IST.2013.6729698

- [46] C.-Y. Yu and S.-S. Yu, "Automatic Localization of the Optic Disc Based on Iterative Brightest Pixels Extraction," in *2014 Int. Symp. Comput. Consumer Control*, 2014. DOI: 10.1109/IS3C.2014.166
- [47] A. D. Fleming, K. A. Goatman, S. Philip, J. A. Olson and P. F. Sharp, "Automatic detection of retinal anatomy to assist diabetic retinopathy screening," *Physics in Medicine and Biology*, vol. 52, no. 2, pp. 331-345, January 2007.
- [48] H. Ying, M. Zhang and J. Liu, "Fractal-based Automatic Localization and Segmentation of Optic Disc in Retinal Images," in *Proc. 29th Annu. Int. Conf. IEEE Eng. Med. Biol. Soc.*, 2007. DOI: 10.1109/IEMBS.2007.4353247
- [49] J. Park, K. N.T. and G. Lee, "Optic Disc Detection in Retinal Images using Tensor Voting and Adaptive Mean-Shift," in *2007 IEEE Int. Conf. Intell. Comput. Commun. Process.*, 2007. DOI: 10.1109/ICCP.2007.4352167
- [50] R. M. Rangayyan, X. Zhu, F. J. Ayres and A. L. Ells, "Detection of the Optic Nerve Head in Fundus Images of the Retina with Gabor Filters and Phase Portrait Analysis," *J. Digital Imaging*, vol. 23, no. 4, pp. 438-453, August 2010. DOI: 10.1007/s10278-009-9261-1
- [51] A. Osareh, M. Mirmehdi, B. Thomas and R. Markham, "Comparison of Colour Spaces for Optic Disc Localisation in Retinal Images," in *Proc. 16th Int. Conf. Pattern Recognition*, 2002. DOI: 10.1109/ICPR.2002.1044865
- [52] H. Li and O. Chutatape, "Automated Feature Extraction in Color Retinal Images by a Model Based Approach," *IEEE Trans. Biomed. Eng.*, vol. 51, no. 2, pp. 246-254, February 2004. DOI: 10.1109/TBME.2003.820400
- [53] M. Foracchia, E. Grisan and A. Ruggeri, "Detection of Optic Disc in Retinal Images by Means of a Geometrical Model of Vessel Structure," *IEEE Trans. Med. Imag.*, vol. 23, no. 10, pp. 1189-1195, October 2004. DOI: 10.1109/TMI.2004.829331
- [54] S. Lu, "Automatic Optic Disc Detection using Retinal Background and Retinal Blood Vessels," in *2010 3rd Int. Conf. Biomedical Eng. Informatics*, Yantai, 2010. DOI: 10.1109/BMEI.2010.5639660
- [55] D. Zhang and Y. Zhao, "Novel Accurate and Fast Optic Disc Detection in Retinal Images with Vessel Distribution and Directional Characteristics," *IEEE J. Biomed. Health Informatics*, no. 99, 28 October 2014. DOI: 10.1109/JBHI.2014.2365514
- [56] The American Academy of Ophthalmology, 2014. [Online]. Available: <http://www.aao.org/aao/>.
- [57] R. Thomas, K. Loibl and R. Parikh, "Evaluation of a Glaucoma patient," *Indian J. Ophthalmology*, vol. 59, no. 7, pp. 43-52, 2011. DOI: 10.4103/0301-4738.73688
- [58] M. Fingeret, F. A. Medeiros, R. Susanna and R. N. Weinreb, "Five rules to evaluate the optic disc and retinal nerve fiber layer for glaucoma," *Optometry*, vol. 76, no. 11, pp. 661-668, November 2005. DOI: 10.1016/j.optm.2005.08.029
- [59] L. G. Nyul, "Retinal Image Analysis for Automated Glaucoma Risk Evaluation," *Proc. SPIE: Medical Imaging, Parallel Process. Images, Optimization Techniques*, vol. 7497, pp. 1-9, October 2009. DOI: 10.1117/12.851179
- [60] R. R. A. Bourne, "The Optic Nerve Head in Glaucoma," *Community Eye Health Journal*, vol. 19, no. 59, pp. 44-45, 2006.
- [61] Z. Zhang, C. K. Kwok, J. Liu, C. Y. L. Cheung, T. Aung and T. Y. Wong, "Automatic Glaucoma Diagnosis with mRMR-based Feature Selection," *J. Biometrics & Biostatistics*, pp. 1-8, 2012. DOI: 10.4172/2155-6180.S7-008
- [62] Japan Glaucoma Society, Guidelines for Glaucoma, 2nd ed., Tokyo: Japan Glaucoma Society, 2006.
- [63] Y. Hatanaka, C. Muramatsu, A. Sawada, T. Hara, T. Yamamoto and H. Fujita, "Glaucoma Risk Assessment Based on Clinical Data and Automated Nerve Fiber Layer Defects Detection," in *34th Ann. Int. Conf. IEEE EMBS*, San Diego, California, 2012. DOI: 10.1109/EMBC.2012.6347352
- [64] Z. Zhang, F. S. Yin, J. Liu, W. K. Wong, N. M. Tan, B. H. Lee, J. Cheng and T. Y. Wong, "ORIGA-light: An Online Retinal Fundus Image Database for Glaucoma Analysis and Research," in *32nd Ann. Int. Conf. IEEE EMBS*, Buenos Aires, 2010. DOI: 10.1109/IEMBS.2010.5626137
- [65] R. Sihota, G. Srinivasan, T. Dada, V. Gupta, D. Ghate and A. Sharma, "Is the ISNT rule violated in early primary open-angle glaucoma - a scanning laser tomography study," *Eye*, vol. 22, pp. 819-824, 2008. DOI: 10.1038/sj.eye.6702798
- [66] Root Eye Network, [Online]. Available: <http://www.opthobook.com/questions/question-what-is-the-isnt-rule-in-glaucoma>.
- [67] C. Muramatsu, Y. Hayashi, A. Sawada, Y. Hatanaka, T. Hara, T. Yamamoto and H. Fujita, "Detection of retinal nerve fiber layer defects on retinal fundus images for early diagnosis of glaucoma," *J. Biomedical Optics*, vol. 15, no. 1, pp. 1-7, February 2010. DOI: 10.1117/1.3322388
- [68] T. Kubena, M. Kofronova and P. Cernosek, "Nerve Fiber Layer Defects Imaging in Glaucoma," in *The Mystery of Glaucoma*, T. Kubena, Ed., InTech, 2011, pp. 187-198. DOI: 10.5772/1028